



The fundamental relationships between grain orientation, deformation-induced surface roughness and strain localization in an aluminum alloy

M.R. Stoudt^{a,*}, L.E. Levine^a, A. Creuziger^{a,b}, J.B. Hubbard^a

^a NIST Center for Metal Forming, Materials Science and Engineering Laboratory, National Institute of Standards and Technology, 100 Bureau Drive, Gaithersburg, MD 20899, United States

^b Kent State University, Kent OH 44242, United States

ARTICLE INFO

Article history:

Received 15 February 2011

Received in revised form 17 June 2011

Accepted 7 September 2011

Available online 24 September 2011

Keywords:

EBSD

Mechanical characterization

Aluminum alloys

Sheet forming

Plasticity

ABSTRACT

Polycrystalline AA6022 tensile specimens were cut from sheet stock, mechanically polished, and uniaxially strained *in situ* under a scanning laser confocal microscope (SLCM) using a sub-sized universal testing apparatus. Prior to deformation, electron backscatter diffraction (EBSD) was performed on the gauge sections of one specimen in the rolling direction of the sheet and one in the transverse direction. Maps of the largest displacements in the surface morphology were constructed from the SLCM data and overlaid onto maps derived from the crystallographic orientation data to examine the strength of the influence that grain orientation effects have on critical strain localization. The roles of Taylor factors, grain boundary misorientation, largest Schmid factors, grain sizes, coincident site lattice orientations, and local grain breakup were considered. The largest surface displacements were observed to be concentrated at triple junctions where there is a large difference between the Taylor factors of the individual grains. The high degree of correlation between the density and location of these large surface displacements and the local plasticity conditions indicate that a critical localization event is most likely to initiate in grain boundary regions where unfavorable slip interactions produce the largest plastic strains.

Published by Elsevier B.V.

1. Introduction

In recent years, numerical predictions of formability have become major components of the design process in the automotive industry. This transition to digital design has increased the demand for accurate and reliable property data that describe the mechanical behavior of metal sheet under a wide range of deformation conditions. This need is particularly acute for new high strength/low weight alloys designed to reduce gross vehicle weight and increase overall vehicle fuel economy. However, the inability to reliably model the evolution of the surface heterogeneities produced during sheet metal forming remains a significant obstacle impeding the widespread incorporation of these poorly understood materials.

Formability simulations are extremely complex and are typically based on phenomenological constitutive relations that assume the response to an imposed macroscopic strain is homogeneous at the microstructural level up to the onset of localization [1]. Accordingly, a significant deviation from the homogeneous response can signify the onset of a critical localization event (i.e., a direct precursor to failure modes such as the formation of a crack

or split, a neck, etc.) [2]. The incorporation of revised plasticity and kinematic hardening models, as well as the results from numerous studies examining the influence of metallurgical parameters such as grain size, grain orientation, and surface roughness, has greatly enhanced the reliability of the data used by the numerical models that predict limiting strains [3–9]. Despite these improvements, large inconsistencies still exist between numerically predicted mechanical behavior and what is observed experimentally. In light of the fact that plastic deformation in a polycrystalline alloy is extremely complex, and that the evolved surface results from many factors, fundamental studies that either relate metallurgical factors for a particular alloy to a performance limiting parameter (e.g., strain localization) or improve the reliability of the material data are essential to improve reliability of the predicted formability.

This paper is part of a series of assessments of the strain localization behavior in commercial aluminum sheet [10–12]. The approach for this research is inspired by the work of Frost and Ashby [13], and others [14], in that changes in the microstructure, or in this case the surface morphology, can be “mapped” with respect to the level of plastic deformation. The results from the earlier studies demonstrated that integrating high-resolution topographical imaging and rigorous matrix-based statistical analysis methods could capture the subtleties of the microstructural conditions that promote a failure event in a relatively simple probabilistic expres-

* Corresponding author. Tel.: +1 3019756025; fax: +1 3019754553.

E-mail address: stoudt@nist.gov (M.R. Stoudt).

sion. A key component in this approach is extending a linear surface roughness parameter (the peak-to-valley surface roughness) to a matrix form. This particular roughness parameter, R_t , was selected for two reasons: (1) the magnitudes of the local surface extremes must change with increasing strain to the point where they reach a value that directly reflects the conditions required to initiate critical strain localization, (2) the R_t parameter is based on the difference in the magnitudes of two individual values (as opposed to the mean of multiple values) so it is highly sensitive to minute changes in the local surface heights. The previous results also revealed that failure did not occur when an individual R_t value reached the critical condition. Rather, failure required multiple critical R_t values in close proximity to one another. This implies that an additional condition, or set of conditions, is required to initiate failure – the most likely of which is derived from variations in the local grain orientation.

Even though numerous evaluations of the relationship between crystallographic texture and the mechanical properties have been reported in the literature, few have directly evaluated the influence of crystallographic texture on the character of the deformed surface. Raabe et al. [15] evaluated this relationship by examining the influence of the degree of misorientation among sets of neighboring points on the surface as a function of plastic deformation. Their results demonstrated that the heterogeneity of the deformed surface correlated with the changes in crystallographic orientation produced by the plastic strain.

The present study examines the strength of the influence that grain orientation effects have on critical strain localization. The approach adopted for this research integrates R_t -based localization maps with grain orientation analysis and it is expected that combining these two data sets will reveal new details about how the location of the largest R_t values correlates with the variations in crystallographic orientation. The overall objective is to develop a reliable and accurate tool that can be used to probe the fundamental relationships between the local microstructure and deformation-induced surface roughness.

2. Experimental

2.1. Material

The aluminum alloy selected for this study, AA6022-T43, was developed primarily for automotive applications. AA6022 is precipitation strengthened with magnesium and silicon, and the T43 heat treatment was designed to enhance the overall formability [16]. According to the literature, AA6022 typically contains (as mass fraction) 0.61 Mg, 0.9 Si, 0.13 Fe, 0.07 Cu, 0.07 Mn, 0.02 Ti, and 0.01 Zn [17]. Metallographic examination revealed that the mean grain size for this alloy was nominally 30 μm and that the grain structure was relatively equiaxed in the rolling plane and slightly elongated along the rolling direction of the sheet (RD). This is consistent with the microstructure normally associated with a solution heat-treated, naturally aged (T) condition [18,19].

Sub-sized, flat tensile specimens were cut from a single 1 mm thick sheet with a water jet cutting tool. The nominal dimensions of the specimens used for these experiments are shown in Fig. 1. Specimens were cut with the tensile axis both parallel to the rolling direction of the sheet (hereafter referred to as RD) and perpendicular to the rolling direction of the sheet (hereafter referred to as TD).

Industry customarily uses sheet stock in the as-received condition with a specified maximum acceptable initial surface roughness that varies with the particular application. While it is always important to emulate material performance under actual forming conditions, the mill scale that forms on the surface of most commercial aluminum alloys during processing completely obscures

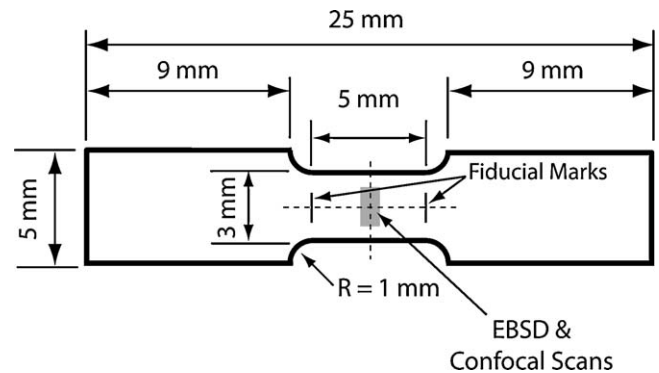


Fig. 1. The geometry of the tensile specimen used with the sub-sized screw driven universal testing apparatus. The approximate locations of the EBSD and SLCM scans are indicated.

the fine surface features that evolve during the initial stages of the deformation process, making high-resolution measurements of these characteristics extremely difficult. So, the specimens in this evaluation were polished to reveal the surface character at low strains, to produce more consistent surface roughness measurements, and to facilitate orientation measurements using electron backscatter diffraction (EBSD). Surface preparation was based on standard metallurgical practice [20] and consisted of mechanically polishing one side to a 0.25 μm diamond finish. The specimens were then placed in a vibratory polisher with a colloidal silica suspension for 2 h. The result was a brilliant surface with no mechanical damage layer that could influence the grain orientation measurements. Upon completion of the polishing, the significant dimensions of each specimen were determined with a linear encoded measuring microscope with a (X, Y, Z) resolution of $\pm 0.5 \mu\text{m}$. In addition, two fiducial lines were lightly scribed outside the uniform gauge length (see Fig. 1) of the specimen to facilitate accurate strain measurements. The distance between these marks was also determined with the measuring microscope.

Electron backscatter diffraction measurements were performed on the gauge sections of the tensile samples prior to deformation. Orientation data were acquired as a beam scan in the center region of the specimen (see Fig. 1) with a JEOL¹ 6400 scanning electron microscope (SEM) using a LaB₆ filament, and HKL EBSD software. EBSD maps were recorded using a 20 keV excitation voltage, a 28 mm working distance, a 400 \times magnification, and a 70 $^\circ$ specimen tilt. Each map was acquired with the tensile axis oriented parallel to the vertical axis of the scan with a 3 μm step size. Sampling the relatively large gauge area of these specimens required stitching the series of 25 (5 maps \times 5 maps) EBSD maps together. Stitching the maps together required manual alignment of each map. As such, an offset of 1–3 pixels (pixels in this case are equivalent to the EBSD step size of 3 μm) is likely between each map. After stitching, a ‘clean up’ procedure was applied to the images to fill in unindexed points and delete points, which is due to mis-indexing of the EBSD pattern did not match the average grain orientation. The clean up procedure used was an initial removal of all spikes (i.e., single pixels of an orientation different than the surrounding 8 pixels) and then an iterative fill-in by 8, 7, 6, 5, and 4 nearest neighbors in sequence. The hit rates for the as-received condition were high for the two samples investigated here (93.0% for TD and 86.8% for RD) so the clean up procedure should not bias the grain

¹ Certain commercial equipment, instruments, software, or materials are identified in this paper to foster understanding. Such identification does not imply recommendation or endorsement by the National Institute of Standards and Technology, nor does it imply that the materials or equipment identified are necessarily the best available for the purpose.

orientation measurements. In addition, the TD sample was reanalyzed after deformation, which resulted in a lower hit rate (66%) due to the plastic deformation.

2.2. Mechanical deformation

Uniaxial straining of the specimens was performed with a sub-sized screw driven universal testing apparatus that was designed for *in situ* mechanical experiments in an SEM. Because of its size, this rig easily fit on the stage of a scanning laser confocal microscope (SLCM). After carefully mounting a polished specimen in the grips, the tensile apparatus was positioned under the 10× objective of the SLCM. Each grip in this testing system is mounted on a separate crosshead and the gearing of the load train is designed to actuate both crossheads symmetrically about the center of the load frame. This arrangement creates a region of the specimen that is stationary with respect to the displacement of the grips. That is, there is a small region (shown in gray in Fig. 1) in the geometric center of the specimen that does not move during straining. Therefore, using this tensile stage enables acquisition of high-resolution images of the specimen surface as a function of the deformation level. The key step in this process is positioning this stationary region in the exact center of the field of view.

Each specimen in this analysis was strained with a crosshead displacement of 0.1 mm/s. A set of calibration experiments was used to determine the set of ten displacements at which the surface conditions would be assessed. When the output of the linear variable displacement transformer (LVDT) reached one of these predetermined displacement values, the stage was held static for a period of 420 s to allow the load to reach a steady state value. The classic shapes of the load drops followed immediately by increased strength during subsequent straining are attributed to dislocation relaxation processes under constant load and simultaneous migration of solute atoms to the dislocation cores, as described recently for a 7000 series alloy [21]. Once the load stabilized, the topography could be assessed with SLCM.

2.3. Surface roughness measurements

All of the SLCM images were acquired in the aforementioned stationary region of the specimen and they were created with a 635 nm red laser source. The spacing between sampling points in the (x, y) plane was fixed by the objective lens at 1.562 $\mu\text{m}/\text{point}$, which generated 640 pixel \times 512 pixel image maps with nominal physical dimensions (x, y, z) of 1000 $\mu\text{m} \times$ 800 $\mu\text{m} \times$ 50 μm . The spacing between the individual focal planes in the z dimension was nominally 400 nm. As described previously [22], the SLCM stores each topographic image as a raw depth map in tagged image file format (TIFF) that contains the complete set of imaging parameters and binary pixel values. The raw binary depth maps were converted into simple matrices describing the x, y and z dimensions of the physical surface, which were then trimmed to square 512-row \times 512-column arrays to facilitate the matrix-based mathematical operations. Using the aforementioned x - y pixel spacing, the values in each matrix correspond to an 800 $\mu\text{m} \times$ 800 μm area of the surface.

Each image was corrected for flatness by computing the optimal equation of the Euclidean plane for each matrix with multiple regression analysis and then subtracting that plane from each point in the image matrix. Next, the extreme values (defined as the values in the height data greater than $\pm 6\sigma$, where σ is the standard deviation of all the height values in that matrix) were screened from the data sets. This step was required because some of the statistical parameters used to interpret the surface data are highly sensitive to outlier data points. Any individual height value that exceeded the $\pm 6\sigma$ threshold was reset to the mean value for that particular

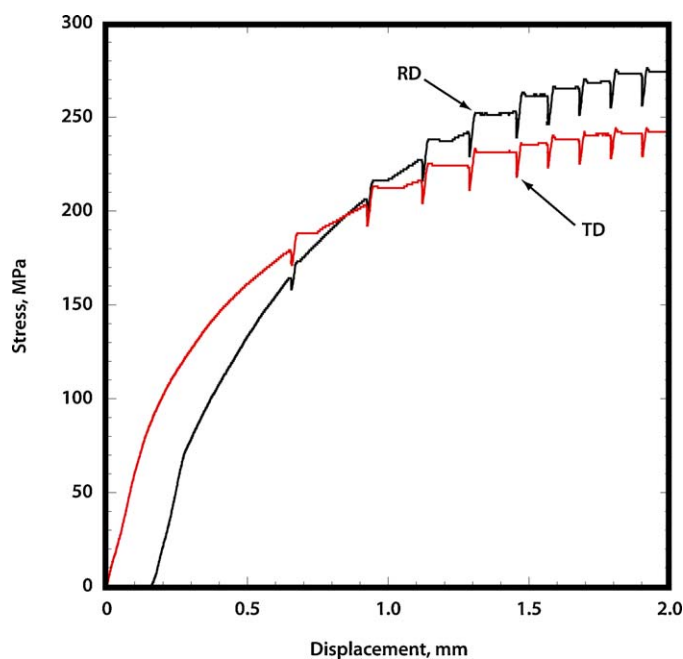


Fig. 2. Stress versus displacement curves for the RD and TD specimens. The drops in stress indicate the levels at which the surface roughness was evaluated. Note that the displacement offset exhibited by the RD specimen was attributed to backlash in the load train at the start of the test.

surface. Note that the number of affected data points for a given surface was typically less than 20 points (or $<0.008\%$ of the total number of data points within the matrix). The resulting residual matrices were used as the source for all subsequent assessments of the surface character.

3. Analysis methods and results

3.1. Deformation-induced topography analysis

The mechanical behavior of the AA6022-T43 in the RD and TD orientations is shown in Fig. 2. The stress drops observable in each of the two curves directly correspond to the displacements at which the surfaces were assessed. A small offset is observable in the RD orientation displacement data, which resulted from backlash in the load train at the start of the test. Considering that the strain values were based on the measured displacement of the fiducial marks, and not on the raw displacement data shown in the figure, this offset is of little consequence.

The evolution of the deformation-induced surface is shown for the TD specimen in Fig. 3 and for the RD specimen in Fig. 4. Both figures exhibit the character of the stationary region at 10%, 15%, 22% and 26% engineering strain. Note that all of the images have an associated error of approximately $\pm 0.5\%$ strain. In addition, the highest strain value shown, 26% strain, exhibits the surface conditions at the onset of critical strain localization (i.e., necking). This is the key surface condition because it represents the topographical structure just before the initiation of the failure event. Since the images presented in both figures show the surface morphologies at essentially the same strain levels, these figures also illustrate the strength of the influence that tensile axis orientation has on the overall character of the surface. While some slip-based deformation is observable at the lower strains, the surfaces shown in Figs. 3 and 4 are mostly composed of grain boundary-localized deformation. This is slightly accentuated in the TD orientation (Fig. 3). As the strain increases, the composition of the deformation becomes a more even distribution of grain boundary-localized and slip-based deformation. This

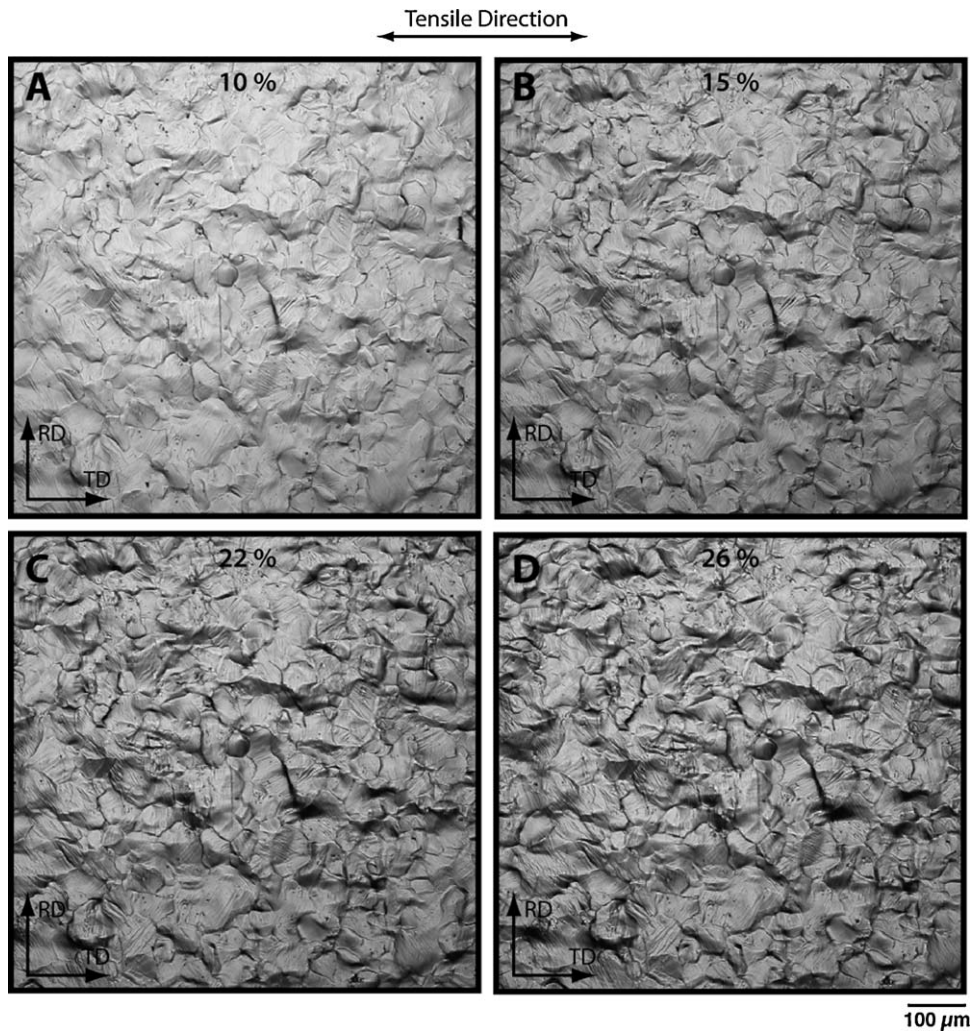


Fig. 3. A scanning laser confocal micrograph showing the surface morphology evolution as a function of uniaxial strain for the AA6022 alloy in the T43 heat treatment: (a) at 10% strain, (b) at 15% strain, (c) at 22% strain and, (d) at 26% strain (just prior to fracture). The tensile direction is perpendicular to the rolling direction (TD orientation) in this figure.

behavior is consistent with the observations reported in a previous study performed on AA5052 [23].

3.2. Strain localization analysis

Quantification of the relationship between surface roughness and strain localization requires a measure that describes the local changes in the magnitudes of the peaks and valleys on the surface [11]. The parameter chosen for this analysis is the maximum profile height, R_t , which is defined as the total vertical distance between the highest and the lowest points of a profile within a particular evaluation length [24]. That is:

$$R_t = R_p + R_v \quad (1)$$

where R_p is the absolute distance between the highest point of the profile and the mean line, and R_v is the absolute distance between the lowest point of the profile and the mean line within a particular evaluation length. (note that heights lower than the mean plane are traditionally shown as negative). Because of the high level of sensitivity to changes in surface height, the R_t parameter is an ideal tool to characterize the surface conditions that promote critical strain localization and to quantify the magnitudes of those surface conditions.

Extending the R_t parameter to a matrix form minimizes the inherent statistical uncertainty associated with profile-based analysis [10,11]. This is accomplished by constructing a Euclidean distance matrix [25], which divides the 512-row \times 512-column source matrix into smaller sub-matrices, or cells, each consisting of 2 pixels/row \times 2 pixels/column. The result is a differential matrix consisting of 65,536 elements (i.e., 256 cells \times 256 cells). The maximum difference in the surface height for any given cell, $R_{t(i,j)}$, was determined from the set of 4 height values contained within that cell. Thus, each $R_{t(i,j)}$ value is the absolute value of the maximum displacement normal to the mean plane at the matrix coordinates of that cell. This construction is equivalent to plotting the maximum measured vertical slope as a function of position on the surface. Since the matrix format preserves the spatial coordinates for each R_t cell by construction, this technique directly links any feature(s) in the topography to the corresponding change in magnitude of the local surface height.

An example showing the R_t matrix construction as well as the relationship of this matrix to the original topography is presented for the TD orientation at 26% strain in Fig. 5. Note that the topography, Fig. 5a, is the same image shown in Fig. 3d except that the 8-bit grayscale is now based on the range of measured surface heights instead of the local intensity of the reflected light. Fig. 5b is the R_t map that was constructed from the topography (Fig. 5a).

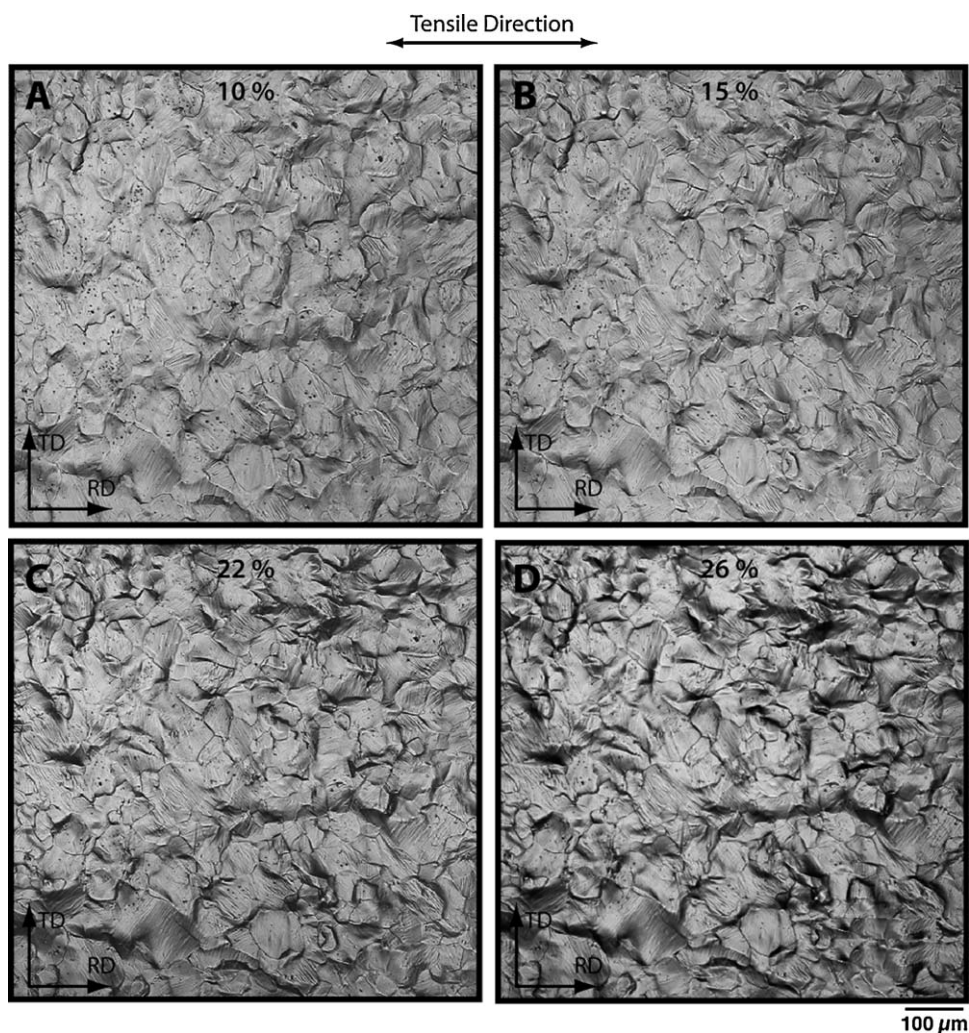


Fig. 4. A scanning laser confocal micrograph showing the surface morphology evolution as a function of uniaxial strain for the AA6022 alloy in the T43 heat treatment: (a) at 10% strain, (b) at 15% strain, (c) at 22% strain and, (d) at 26% strain (just prior to fracture). The rolling direction is parallel to the tensile direction (RD orientation) in this figure.

A previous study showed that the R_t data are well characterized with a Weibull distribution [12]. Weibull statistics are often used to estimate failure because they emphasize the incidence of statistically rare events (i.e., those that lie in the tail regions of a distribution). The Weibull distribution is commonly expressed in terms of the cumulative distribution function (CDF) because in this form, the expression enables a straightforward estimate of the failure probability [26]:

$$f_{CDF}(x; \alpha, \beta) = 1 - e^{-(x/\alpha)^\beta}. \quad (2)$$

In this equation, $x \geq 0$ and $f_{CDF}(x; \alpha, \beta) = 0$ for $x < 0$. The 2 parameters, a scale parameter (α), and a shape parameter (β), must be real, and >0 . Thus, for any given strain level, the CDF is the probability, P , of the occurrence of an R_t magnitude that is less than or equal to a given R_t i.e., $f_{CDF}(R_{t \text{ given}}) = P(R_t \leq R_{t \text{ given}})$. In addition, the CDF is bounded by the following conditions: $f_{CDF}(0) = 0$, and $f_{CDF}(\infty) = 1$.

The statistically rare events in the tail of the R_t distribution are particularly germane to this analysis because the largest magnitudes in the R_t distribution reflect the highest probability that the surface conditions will promote strain localization and/or failure [10]. For this analysis, the tail was defined as the segment of the R_t distribution where the R_t magnitudes have a probability ≥ 0.95

based on the CDF constructed from the R_t data set with Eq. (2). In this case, the 0.95 threshold corresponds to an R_t value of $3.0 \mu\text{m}$. By filtering the values $< 3.0 \mu\text{m}$ from the R_t map, one can gain insight about how these 'extreme' R_t values are distributed with respect to the surface morphology at failure. As such, Fig. 5c shows the locations of the R_t values after the values $< 3.0 \mu\text{m}$ have been removed. This figure was generated by mapping the range of R_t magnitudes into a standard 8-bit color scale, where blue (For interpretation of the references to color in this text, the reader is referred to the web version of the article.) is low and red is high, so that the color of an individual cell directly indicates the magnitude of R_t . Fig. 5d is a composite image created by overlaying the filtered R_t map (Fig. 5c) onto Fig. 5a. As expected, the remaining R_t values in this figure mostly surround the largest surface features. While some of these R_t values correlate with slip-based (i.e., intra-grain) surface roughening, the figure is consistent with previous observations in that most of the surface displacements tend to occur along grain boundary regions [23,27–29].

The results from the EBSD-based grain orientation analysis are shown for the TD and RD specimens in the as-polished condition in Fig. 6a and b, respectively. Each map displays the grain orientation of the sample normal direction in a typical inverse pole figure triangle. The color key indicates that while the grain orientations are,

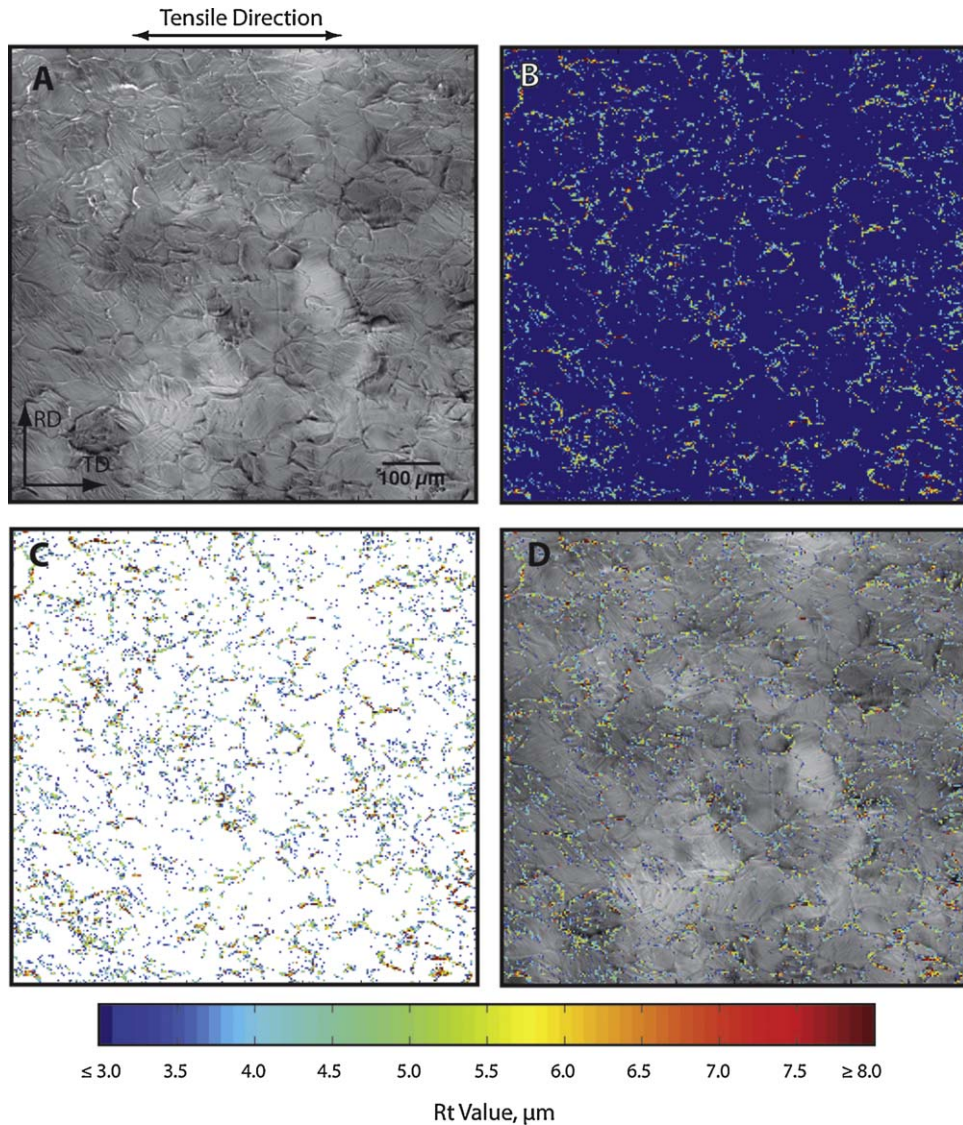


Fig. 5. An example of the method used to construct the R_t overlay from the TD topography data: (a) The surface from Fig. 3d shown as a topography, (b) the R_t map constructed from (a), (c) the R_t map shown in (b) after all values < 3.0 (a 0.95 probability threshold) have been eliminated and, (d) the composite figure resulting from overlaying (c) on (a).

for the most part, uniformly distributed, there is a slight tendency toward the (001) orientation (red). Additional grain size analysis performed with EBSD indicated that the variability in the grain size was on the order of $\pm 20 \mu\text{m}$ from the nominal grain size of $30 \mu\text{m}$. This relatively wide dispersion is observable in the EBSD maps from both specimens. No further textural analysis was performed on either specimen because of the small number of grains in the measurements (1080 grains for the TD sample, and 870 grains for the RD sample).

Fig. 7 is an overlay of the EBSD map of the TD orientation (Fig. 6a) over the composite topography/ R_t map (Fig. 5d). Finding the congruent regions in these two images presented two significant challenges. First, the EBSD scans contain substantial distortion due to the strain applied to the sample (EBSD was performed prior to straining), the cumulative misalignment produced by stitching the individual images together, the distortion resulting from tilting the surface to 70° with respect to the incident electron beam, and the aberrations present in the magnetic lenses. Thus, the shape and size of each grain shown in Fig. 6 was considerably different from the plan view exhibited in Figs. 3 and 5. Compensating for

this difference required a stretch, shear, and rotation operation on the EBSD image to place the two images in phase. A set of distinct grains common to both images (labeled in the figure as α , β , etc.) was used to facilitate this correction. The second challenge was compensating for the difference in scan areas. While the scan areas were nominally in the exact center of the sample, there was a slight offset, and this is reflected in Fig. 7. The overlapped region, highlighted with a black line, is the area where the topography and the EBSD images are congruent, and based on this figure, the offset between the EBSD y-axis (bounding line to the left) and the tensile axis of the sample is 4° . As before, the R_t map overlay indicates the location of the largest R_t magnitudes with respect to the topography; but with the addition of the EBSD overlay, one can now directly correlate a specific topographic feature with the local microstructural conditions that produced it. Fig. 8 is a similar construction for the RD orientation; however, the offset between the EBSD and tensile axes is 8° . Also the congruent region shown in this figure is noticeably smaller than that shown for the TD orientation.

It is well known that the differences in crystal orientation within a polycrystalline material produce variations in the local yield

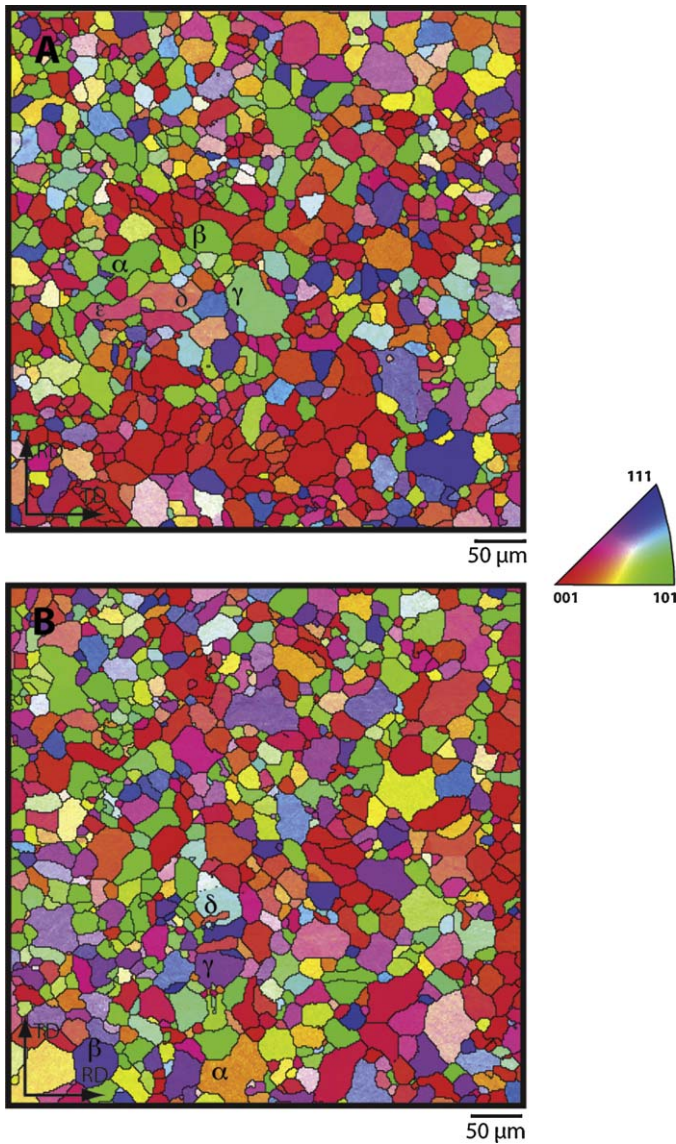


Fig. 6. The sample normal orientation maps for the (a) TD and (b) RD specimens in the as-polished, undeformed condition. The grains (labeled α , β , γ , etc.) in each figure were used to facilitate construction of Rt -orientation overlays. A standard tri-color inverse pole figure for cubic materials is also shown in the figure.

criteria. One common approach to assess these variations is to determine the differences in the local plastic flow conditions by computing the individual Taylor factors. Taylor [30] made the simplifying assumption that all of the grains in a polycrystal would deform identically, thus maintaining compatibility. Mises [31] had earlier pointed out that at least five independent strain components were required to plastically deform a (constant volume) solid without geometric restrictions and Taylor hypothesized that five slip systems would be active in each grain.² Since there are more than five combinations of slip systems available in fcc materials, additional criteria were required. Taylor [30] further hypothesized that the slip systems that are active during plastic deformation are those that minimize the internal work. Taylor then made the assumptions that the critical shear stress, τ_0 , for all slip systems is the same and that work hardening does not vary between grains. Thus,

² The assumption that exactly five slip systems would be active only applies under the assumptions made by the full constraints Taylor model. If this assumption is relaxed, then different numbers of slip systems can be active.

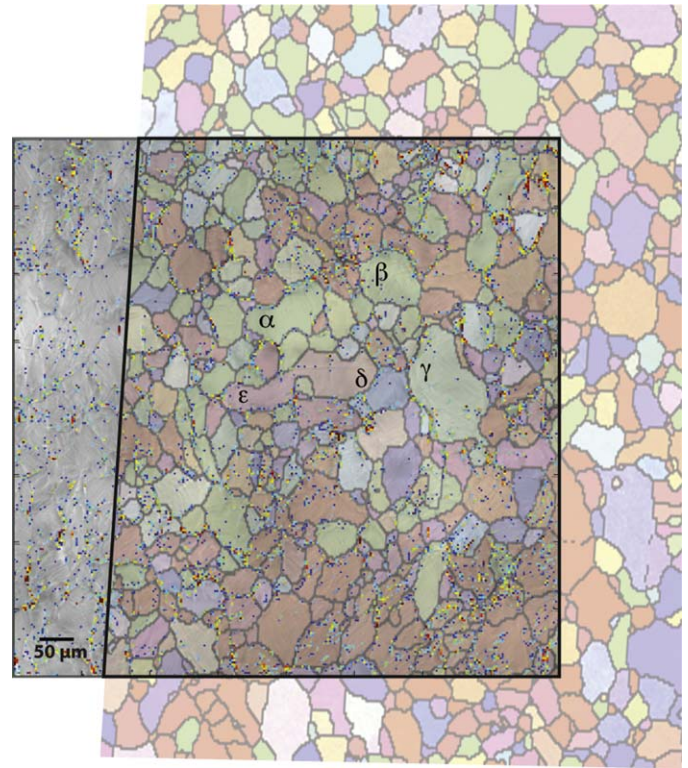


Fig. 7. The composite image produced by overlaying Fig. 6a on top of Fig. 3d. The area bounded by the black line is the region where both images are congruent.

minimizing the internal work becomes equivalent to minimizing the total incremental crystallographic shear for a given grain:

$$da = \sum_{i=1}^5 da_i \quad (3)$$

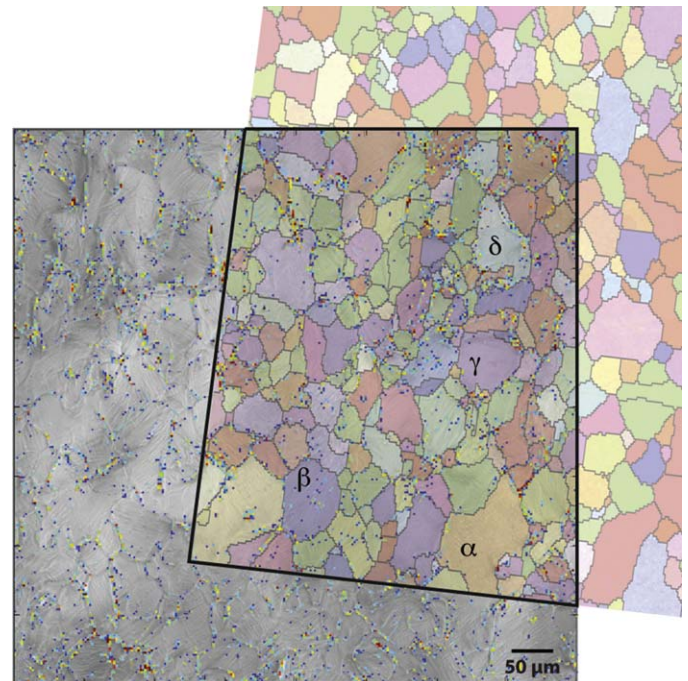


Fig. 8. The composite image produced by overlaying Fig. 6b on top of Fig. 4d. The area bounded by the black line is the region where both images are congruent.

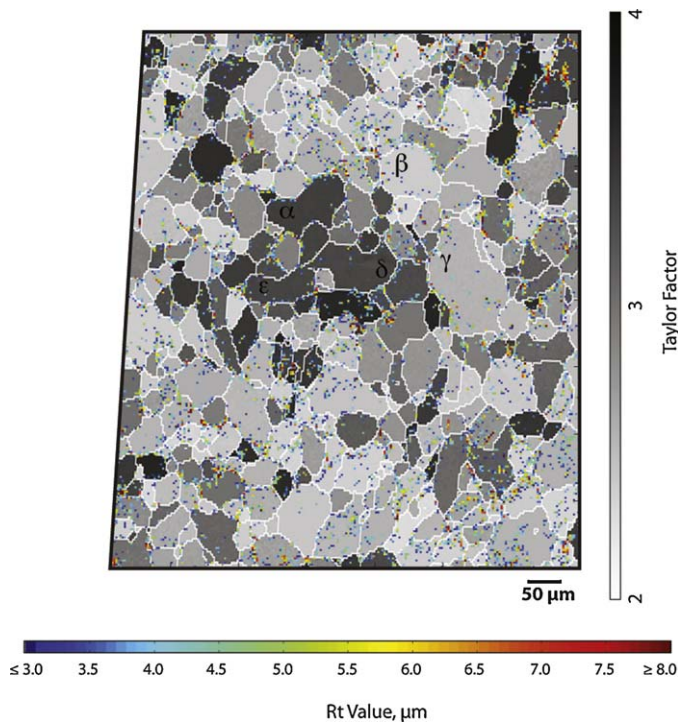


Fig. 9. The congruent region of the image produced by overlaying the R_t composite image in Fig. 3d on top of a Taylor map that was constructed from the orientation data shown in Fig. 6a.

where da_i is the incremental shear strain on slip system i . The increment of internal work then becomes $dW = \tau_0 da$, which can be equated with the external work, $dW = \sigma d\varepsilon$, where σ is the macroscopic tensile stress and $d\varepsilon$ is the corresponding incremental macroscopic strain. The result is

$$\frac{\sigma}{\tau_0} = \frac{da}{d\varepsilon} = M, \quad (4)$$

where M is the Taylor factor. For fcc metals, the average M is approximately 3.1. For a more detailed treatment of Taylor factors, see [32] or [33]. Note that the increment of work is proportional to da . Thus, from Eq. (4) we see that for a given increment of applied tensile strain, a large Taylor factor corresponds to a grain that requires a large amount of plastic work to deform and is therefore “stronger”. Of course, this calculation is based on the assumption that all grains deform identically in simple uniaxial tension with no regard to complex neighbor interactions.

Figs. 9 and 10 are maps of the Taylor factors for the TD and RD orientations, respectively. Both maps were computed from the EBSD data using the TaylorCubicY.dll toolbox within the HKL crystallographic software suite. This routine assumes that the tensile axis is parallel to the y -axis of the EBSD scan, and as noted previously, this is only approximately correct (4° and 8° offsets for TD and RD respectively). The corresponding R_t maps are overlaid upon the Taylor factor maps. As in the case of the R_t -EBSD overlays shown in Figs. 7 and 8, the areas shown in both figures are the regions where the Taylor factor maps and the R_t -overlays are congruent. One distinct difference between Figs. 9 and 10 is the higher density of R_t values in Fig. 9 (the TD orientation). The R_t values appear to be more concentrated in the grain boundary regions, which is consistent with the behavior shown in Figs. 3 and 4.

The relationship between the grain orientation and the morphology of the deformed surface is shown at a higher magnification for the TD orientation in Fig. 11. Fig. 11a shows a SLCM image of this region where some of the more distinctive grains are again indicated by (α , β , δ , ε) to match those shown in Fig. 10. The grain

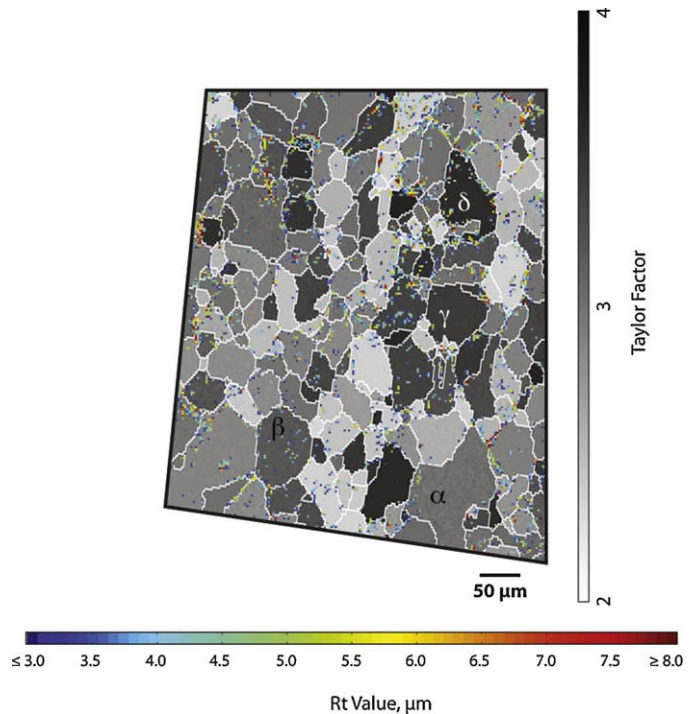


Fig. 10. The congruent region of the image produced by overlaying the R_t composite image in Fig. 4d on top of a Taylor map that was constructed from the orientation data shown in Fig. 6b.

marked γ in Fig. 10 is not included in the figure. EBSD scans were also performed on the samples after deformation. As such, Fig. 11b and c are the TD orientation maps before and after 26% tensile strain, respectively.

We also calculated the local misorientation (also called the kernel average misorientation, or KAM) by calculating the difference in orientation from pixels three steps away in each direction (square) up to an orientation cut off of 5° . These calculations were carried out for the TD sample to investigate the intergranular deformation; the results are presented in Fig. 12.

4. Discussion of results

As described above, the Taylor and R_t maps that are overlaid in Figs. 9 and 10 are not completely contiguous largely due to deformation-induced changes in the grain shapes and cumulative errors in assembling the 25 EBSD maps. Nevertheless, several features are apparent that are common to both the TD and RD samples. First, most of the highest (red) R_t locations occur at triple junctions where there is a large difference between the Taylor factors of the individual grains. This is not surprising since triple junctions are widely recognized as possible stress concentration points and inter-grain deformation is expected to be largest between grains with a large difference in the Taylor factors [34]. Another common feature is that pronounced slip band behavior occurs predominately in grains with low Taylor factor. This is particularly evident in the TD sample (Fig. 9), where the intra-grain slip appears in the upper and lower regions of the figure and the Taylor factor is low. Conversely, the central region of this figure has a collection of grains with much higher Taylor factors, none of which exhibit enough intra-grain slip to appear on the R_t map.

It is tempting to conclude that slip is minimal in grains with high Taylor factor, but this is too simplistic. For example, Fig. 11a shows a high-resolution SLCM image of this same high-Taylor-factor region of the deformed TD sample. Finely distributed slip is clearly evident in the grains that did not show activity on the R_t map. This slip does

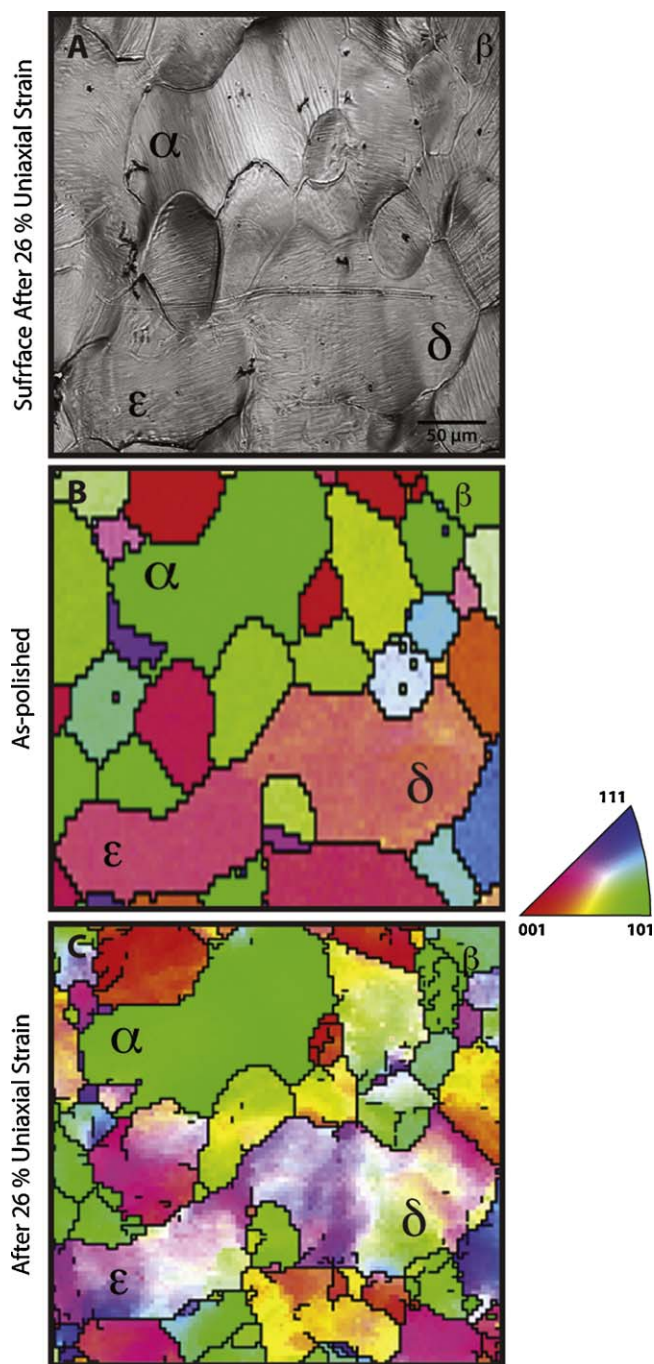


Fig. 11. The surface of the TD specimen shown at a higher magnification to better reveal the relationship between grain orientation and the deformed surface morphology: (a) a SLCM image of the region exhibiting some of the distinctive grains, (b) the TD orientation map before deformation and, (c) the TD orientation map after the application of 26% strain.

not appear because of the criteria used in producing the R_t map: a $100\times$ overall magnification and a 0.95 threshold. That is, if the higher magnification image in Fig. 11b was used as the source for an R_t /Taylor map overlay construction, it is likely that some of the fine slip exhibited in the figure would be observable. In contrast, the lower Taylor factor grains often have slip confined to gross slip bands which have large enough local height changes to exceed the R_t map threshold [35]. In the following, “fine slip” refers to grain-interior slip structures that do not show up on the R_t map.

Another related factor that directly influences the surface roughening is the change in the local grain orientation [15]. Fig. 11b and

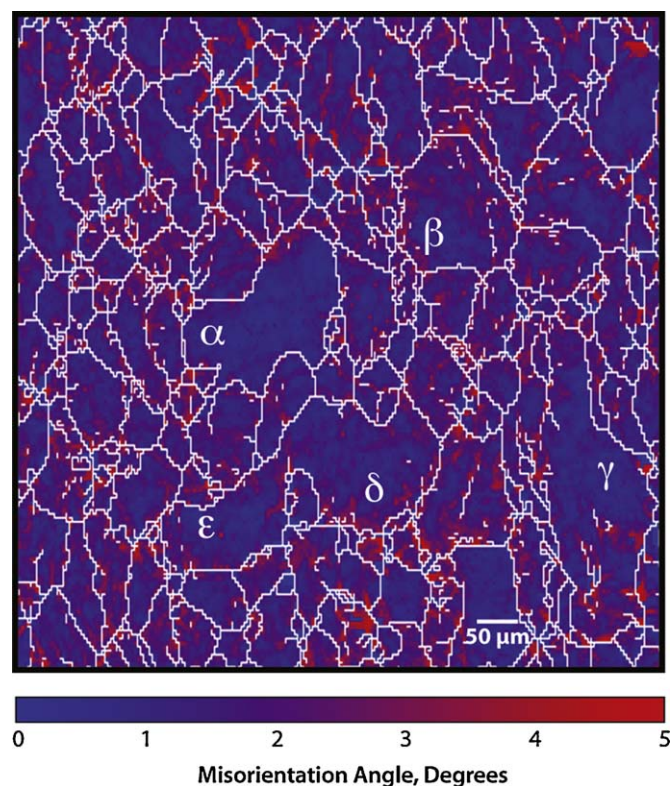


Fig. 12. A map showing the local misorientation (also called the kernel average misorientation or KAM) performed by calculating the average difference in orientation from pixels 3 steps away in each direction (square) up to an orientation cut off of 5° .

c are orientation maps of the same region of the TD sample taken before and after deformation, respectively. The two high-Taylor-factor grains just below the center of this figure (labeled as δ and ϵ) show a broad array of colors, indicative of fine-scale crystal breakup into numerous sub-grains. The fine slip in these grains varies considerably with position, which is consistent with this result. The large grain labeled α in Fig. 11a also displays fine slip; but unlike δ and ϵ , all of the slip lines in α appear to be parallel. This would explain why the grain orientation remained uniform during deformation.

The above observations are consistent with the idea that fine slip is favored in grains with high Taylor factor. Such grains are observed to deform more “smoothly” than those with lower Taylor factor and thus often exhibit larger local intra-grain misorientation, but little intra-grain surface roughness (as defined by the R_t criteria). However, this same ability to deform around obstacles can lead to substantial surface roughening at the grain boundaries. Thus, a grain with high Taylor factor may exhibit a plastic strain “discontinuity” when adjacent to a grain with different primary slip directions or substantially lower Taylor factor. This is consistent with the general pattern of large grain-boundary roughness delineating many of the central high-Taylor factor grains in Fig. 9. Although many of these active grain boundaries occur between grains of similar Taylor factor, inspection of the EBSD map in Fig. 6 shows that the corresponding crystallographic orientations are very different.

Another factor that seems to play some role is the grain size. Smaller grains are generally expected to be stronger than larger grains (Hall–Petch relationship [36]) and inspection of the R_t map overlays in Figs. 7 and 8 demonstrates that the sample regions with the largest R_t values are frequently located on grain boundaries adjacent to the smallest grains (with one dimension below $\approx 15\ \mu\text{m}$).

Finally, the correspondence between changes in local orientation and distributed fine slip in highly deformed grains suggests that an EBSD map showing local misorientation may provide useful information comparable to the R_f map construction. Fig. 12 shows an EBSD-derived map of the local misorientation in the TD sample after 26% plastic strain. As described above, this map shows the local difference in orientation from pixels three steps away in each direction (square) up to an orientation cut off of 5° (which is considered a grain boundary). The brightest red regions in this figure exhibit the largest local misorientation. These regions are primarily restricted to the grain boundaries and they correspond remarkably well with the regions of largest R_f value in Fig. 7. As such, these results contradict the findings of Raabe et al. [15]. They concluded that strain localization is primarily dependent on the local orientation, and therefore, can initiate at grain boundaries and within the interior of grains with similar probability. While Fig. 12 indicates that appreciable changes in the local orientation occurred in most of the grains in the figure, the largest R_f values tended to be concentrated along the grain boundary regions and not in the grain interiors. Considering that the largest R_f values reflect the greatest surface displacements, strain localization is more likely in the grain boundary regions than in the interior. This would agree with the conclusions by Bieler et al. [37] that failure was more likely to initiate along grain boundary regions where unfavorable slip interactions reduced the local strength of the boundary and not in regions with the highest local strain conditions. Based on these results, the overlay mapping approach demonstrated here can be used to evaluate the local conditions in the grain boundary regions to assess the strength of the relationship between the highest surface roughening, the degree of grain misorientation, and the location of failure.

5. Conclusions

The general rules described above are only true in a rough statistical sense, since many exceptions exist. Considering the numerous assumptions made in the Taylor factor analysis, it is quite surprising how well this criterion worked. Other factors, such as grain boundary misorientation, locations of coincident site lattice orientations, and highest Schmid factors were also investigated. These analyses were not presented since the agreement between these parameters and the R_f maps was relatively poor with respect to the Taylor and misorientation maps. Even the Taylor map does not provide adequate information to completely predict the local deformation and roughening behavior of the samples. While the correlation between the surface roughness and the EBSD-derived maps reported here is remarkable, the only microstructural information included in the analysis was the orientation of each grain. The primary factors that are missing from all of these approaches are: (1) information about the subsurface grains, (2) the activity of individual slip systems in each grain and how this affects local inter-grain stresses and strains, and (3) a consideration of how “clusters” of grains affect deformation at the multiple-grain length scale. However, many of these shortcomings can be overcome by combining the unique multiple-technique surface analysis approach described in this paper with crystal-plasticity-based finite element modeling of the deformation experiment. Some attempts have already been made to relate subgrain microstructure with slip activity [38,39] through polycrystalline modeling efforts. Nevertheless, obtaining three-dimensional information about the shapes and orientations of the subsurface grains would require either destructive

measurements (such as serial sectioning) or synchrotron-based X-ray diffraction methods.

Acknowledgement

The authors would like to acknowledge the contributions of S. M. Olson of the Materials Science and Engineering Department at Lehigh University who performed the mechanical tests, as well as the initial SLCM and EBSD measurements. Mr. Olson was supported in part by the National Science Foundation's Research Experience for Undergraduates (REU) program, Division of Materials Research.

References

- [1] T. Pardoen, Y. Brechet, *Philos. Mag.* A 84 (2004) 269–297.
- [2] Z. Marciniak, K. Kuczynski, *Int. J. Mech. Sci.* 9 (1967) 609–620.
- [3] F. Barlat, R.C. Becker, Y. Hayashida, Y. Maeda, M. Yanagawa, K. Chung, J.C. Brem, D.J. Lege, K. Matsui, S.J. Murtha, S. Hattori, *Int. J. Plasticity* 13 (1997) 385–401.
- [4] A.J. Beaudoin, A. Acharya, S.R. Chen, D.A. Korzekwa, M.G. Stout, *Acta Mater.* 48 (2000) 3409–3423.
- [5] R. Becker, O. Richmond, *Model. Simul. Mater. Sci. Eng.* 2 (1994) 439–454.
- [6] H.A. Al-Qureshi, A.N. Klein, M.C. Fredel, *J. Mater. Proc. Tech.* 170 (2005) 204–210.
- [7] J. Savoie, M. Jain, A.R. Carr, P.D. Wu, K.W. Neale, Y. Zhou, J.J. Jonas, *Mater. Sci. Eng. A* 257 (1998) 128–133.
- [8] P.D. Wu, D.J. Lloyd, M. Jain, K.W. Neale, Y. Huang, *Int. J. Plasticity* 23 (2007) 1084–1104.
- [9] W.B. Lievers, A.K. Pilkey, D.J. Lloyd, *Acta Mater.* 52 (2004) 3001–3007.
- [10] M.R. Stoudt, J.B. Hubbard, *Philos. Mag.* A 89 (2009) 2403–2425.
- [11] M.R. Stoudt, J.B. Hubbard, M.A. Iadicola, S.W. Banovic, *Metall. Mater. Trans. A* 40 (2009) 1611–1622.
- [12] J.B. Hubbard, M.R. Stoudt, A. Possolo, *Mater. Sci. & Technol.* 27 (2011) 1206–1212.
- [13] H.J. Frost, M.F. Ashby, *Deformation-Mechanism Maps: The Plasticity and Creep of Metals and Ceramics*, Pergamon Press, Oxford, 1982, p. 166.
- [14] G.W. Greenwood, *Mater. Sci. Eng. A* 410–411 (2005) 12–15.
- [15] D. Raabe, M. Sachtleber, H. Weiland, G. Scheele, Z. Zhao, *Acta Mater.* 51 (2003) 1539–1560.
- [16] Anon., *Aluminum Standards and Data 2003*, The Aluminum Association, Washington, DC, 2003, p.235.
- [17] H.C. Lin, T.Y. Kuo, C.C. Lin, *Metall. Mater. Trans. A* 40 (2009) 2578–2589.
- [18] Anon., *Metallography and Microstructures*, ASM International, Metals Park, OH, 1987, p. 669.
- [19] W.F. Smith, *Structure, Properties of Engineering Alloys*, McGraw-Hill Book Company, New York, 1981, p. 512.
- [20] G.F. VanderVoort, *Metallography Principles and Practice*, ASM International, Materials Park, OH, 1999, p. 752.
- [21] M.A. Choudhry, M. Ashraf, *J. Alloys Compd.* 437 (2007) 113–116.
- [22] M.R. Stoudt, J.B. Hubbard, S.A. Janet, *Mater. Sci. & Technol.* 24 (2008) 253–260.
- [23] M.R. Stoudt, J.B. Hubbard, S. Leigh, *Metall. Mater. Trans. A* 42 (2011) 2668–2679.
- [24] Anon., *ASME Designation B46.1-2002: Surface Texture (Surface Roughness, Waviness and Lay)*, The American Society of Mechanical Engineers, New York, NY, 2002, p. 98.
- [25] J. Dattorro, Chapter 4: Euclidean Distance Matrix, in: *Convex Optimization & Euclidean Distance Geometry*, MeBoo Publishing, USA, Palo Alto, CA, 2005, 219–314.
- [26] Anon., *Weibull distribution*, in: *Wikipedia, The Free Encyclopedia*, 2008.
- [27] M.R. Stoudt, R.E. Ricker, *Metall. Mater. Trans. A* 33 (2002) 2883–2889.
- [28] M.R. Stoudt, J.B. Hubbard, *Acta Mater.* 53 (2005) 4293–4304.
- [29] M.R. Stoudt, J.B. Hubbard, S.P. Mates, D.E. Green, *SAE Trans. J. Mater. & Manuf.* 114–5 (2006) 183–190.
- [30] G.I. Taylor, *J. Inst. Met.* 62 (1938) 307–324.
- [31] R.v. Mises, *Z. Angew. Math. Mech.* 8 (1928) 161.
- [32] H.R. Piehler, *Crystal-Plasticity Fundamentals*, in: *Metals Handbook: Fundamentals of Modeling for Metals Processing*, vol. 22A, ASM International, Metals Park, OH, 2009, 232–238.
- [33] W.F. Hosford, *The Mechanics of Crystals and Textured Polycrystals*, Oxford University Press, Oxford, 1993.
- [34] S.I. Wright, D.P. Field, *Mater. Sci. Eng. A* 257 (1998) 165–170.
- [35] D.E. Kramer, M.F. Savage, L.E. Levine, *Acta Mater.* 53 (2005) 4655–4664.
- [36] N.J. Petch, *J. Iron Steel Inst.* 174 (1953) 25–28.
- [37] T.R. Bieler, P. Eisenlohr, F. Roters, D. Kumar, D.E. Mason, M.A. Crimp, D. Raabe, *Int. J. Plasticity* 25 (2009) 1655–1683.
- [38] B. Peeters, M. Seefeldt, C. Teodosiu, S.R. Kalidindi, P. van Houtte, E. Aernoudt, *Acta Mater.* 49 (2001) 1607–1619.
- [39] S. Mahesh, C.N. Tomé, R.J. McCabe, G.C. Kaschner, I.J. Beyerlein, A. Misra, *Met. Mater. Trans. A* 35 (2004) 3763–3774.